



# Properties of electroless Cu films optimized for horizontal plating as a function of deposit thickness



Tanu Sharma<sup>a</sup>, Ralf Brüning<sup>a,\*</sup>, Tang Cam Lai Nguyen<sup>b</sup>, Tobias Bernhard<sup>b</sup>, Frank Brüning<sup>b</sup>

<sup>a</sup> Physics Department, Mount Allison University, Sackville, New Brunswick E4L 1E6, Canada

<sup>b</sup> Atotech Deutschland GmbH, Erasmustrasse 20, 10553 Berlin, Germany

## ARTICLE INFO

### Article history:

Received 20 December 2014

Received in revised form 16 April 2015

Accepted 24 May 2015

Available online 4 June 2015

### Keywords:

Electroless plating

Internal strain

X-ray diffraction

In-situ strain monitoring

## ABSTRACT

The properties of electroless films produced from a bath designed for horizontal plating, the preferred technology for high production volumes in printed circuit board metallization, are reported. Film thickness, substrate type and electrolyte temperature were varied. Formation of a continuous layer of copper film is correlated with a change in the visual and spectroscopic appearance. Grain orientation is random in thin films and a (110) texture develops with increasing thickness. The plating solution contains Cu and Ni ions. Nickel co-deposits in copper films in the form of Ni hydroxide, and its concentration decreases from about 6% in the vicinity of the substrate to about 1% at the film surface. Film stress and strain were measured by substrate curvature and X-ray diffraction, respectively. Both stress and strain decrease as the film thickness increases. Stress remains tensile throughout during deposition and during relaxation, promoting film adhesion by preventing blisters. After deposition, stress relaxes first towards compressive and then towards tensile. The stress, the stress relaxation and the Ni concentration are high at the base of the film. We attribute this to the higher volume fraction of grain boundaries (smaller grain size) in this region.

© 2015 The Authors. Published by Elsevier B.V. This is an open access article under the CC BY license (<http://creativecommons.org/licenses/by/4.0/>).

## 1. Introduction

Electroless Cu plating is used in the electronics industry to obtain conductive layers on bare resins [1–3]. High-end applications like plating of integrated circuit (IC) substrate interconnects require fine-grained copper to achieve small structures [4]. As plated structures become smaller and substrates smoother, film adhesion is increasingly problematic, and stress data are becoming part of industrial process specifications. Moderate tensile stress is essential for the film adherence to the substrate. Nickel, initially added to the electrolytes in order to improve deposition speed, promotes film adhesion. During plating films without nickel are in a compressive state that can cause blisters. Co-deposition of about 1% Ni in the Cu film prevents compressive stress during deposition [5]. Building upon a model for the stress evolution in pure metal films with high atomic mobility [6], we proposed segregation of the Ni in the grain boundaries (GBs) as the mechanism that suppresses Cu adatom diffusion into the GBs during deposition [7], thus avoiding the compressive regime that in Ni-free deposits can cause blisters during plating [8,9]. In-situ measurements of the average film stress during electroless deposition were carried out for metal substrates and insulating substrates [10,11]. The mechanical state of Cu films on insulating substrates has to be considered carefully [12].

The mechanical problem is complex because a (yielding) polymer substrate is mechanically coupled to a ductile film. Furthermore, in nanocrystalline materials macroscopic stress and Cu crystallite strain are, even in the elastic regime, not coupled directly because of significant elastic or inelastic GB sliding [13]. With the deposit thickness, substrate type and bath temperature as variables, this paper considers stress and strain for films plated from a bath whose performance has been optimized for IC substrate applications and horizontal plating processes at high deposition rates.

## 2. Experimental methods

The Cu films were produced from a commercial electroless plating bath (Printoganth SAP Plus). Table 1 lists the bath components and the operating conditions for optimum performance. Plating on non-metallic surfaces was preceded by cleaning and desmearing steps, and deposition was initiated by palladium nuclei created by the reduction of palladium ions directly on the surface that is to be plated (Pd-activation).

X-ray diffraction (XRD) measurements were carried in symmetric reflection with a custom built  $\theta - \theta$  diffractometer equipped with graphite monochromator and analyzer crystals, and a scintillation detector.  $\text{CuK}\alpha$  radiation was used, and the X-ray tube was operated at 40 kV and 35 mA. Strain was determined by finding the Cu lattice constant  $a(\psi)$  as a function of the angle  $\psi$  between the scattering vector

\* Corresponding author.

E-mail address: [rbruening@mta.ca](mailto:rbruening@mta.ca) (R. Brüning).

**Table 1**  
Components and standard operating parameters of the plating bath.

Component/parameter	Setpoint
Cu	3.0 g/L
Ni	0.5 g/L
Complexer	Tartrate
Reducer	Formaldehyde
Stabilizer	Dipyridyl
Density at 20 °C	<1.085 g/cm <sup>3</sup>
pH	13.6
Temperature	32 °C
Thickness, $h_f$	0.8 μm
Adhesion (0.2 μm ≤ $h_f$ ≤ 0.8 μm)	2.0 ± 0.3 MPa
Resistivity (0.1 μm ≤ $h_f$ ≤ 5.6 μm)	1.7 ± 0.5 μΩ · cm

$\vec{q}$  and the direction normal to the film [5]. The sample was tilted by  $\psi$  about the  $\chi$ -axis, located in the scattering plane and perpendicular to the scattering vector. XRD strain measurements at standard bath operating conditions were carried out in-situ during and after the electroless plating process. Substrates were acrylonitrile butadiene styrene (ABS) coupons (diameter 30.00 mm, thickness 1.25 mm, supplied by Metak GmbH, Burgwald, Germany) that were thinned with a lathe at their centers to 0.23 mm to minimize X-ray absorption. The Pd-activated coupons were mounted on the top of a temperature controlled Plexiglas cell (diameter 7 cm, height 5.5 cm) using Teflon tape as sealant. Plating was initiated by filling the cell with electrolyte using a peristaltic pump, and the electrolyte was circulated through the cell during plating. The X-rays reached the growing film through the thinned ABS coupon. Hydrogen, evolving as part of the electrochemical process, was vented through a tube connected at the highest point of the cell tilted by 17° with respect to the vertical. For rapid measurements during plating, only the Cu (311) peak was monitored alternately at  $\psi = 0^\circ$  and  $\psi = 65^\circ$ . At the end of plating, the cell was drained and rinsed by briefly circulating deionized water. Monitoring of the (311) peak continued for 10 h, followed by measuring all five accessible diffraction peaks at a wider range of sample tilts,  $\psi$ .

Coupons were plated ex-situ with film thicknesses ranging from 0.13 to 7.69 μm at temperatures between 10 and 50 °C. XRD measurements of fully relaxed samples were carried out. Typical relaxation times are less than one day, as shown below. In this case the Cu film faced up, and symmetric reflection measurements of five diffraction peaks were carried out at  $\psi = 0, 20, 40, 60$  and  $80^\circ$ . All experiments were done in pseudo-random sequence.

The time-evolution of average stress in copper films was determined based on the substrate curvature technique. Stoney's equation relates the curvature of the test strip,  $\kappa$ , to the biaxial film stress,

$$\sigma = \frac{E_s h_s^2}{6h_f(1-\nu_s)} \kappa, \quad (1)$$

where  $h_f$  and  $h_s$  are the thicknesses of film and substrate, respectively, and  $E_s$  and  $\nu_s$  are, respectively, the elastic modulus and Poisson's ratio of the substrate [14]. For the purpose of this analysis we assume that the films grow at a constant rate during plating. The Pd-activated samples were mounted on an optical bench in front of a camera. The electroless plating solution was held in a transparent Plexiglas container (8 cm wide, 3 cm thick and 18 cm high). The container with the plating solution was raised to immerse the test strip, and photographs were taken before, during and after plating. Metal test strips for these deposit stress measurements, made from Cu–Fe (alloy 194, 51 μm thick) and Ni–Fe (alloy 42, 38 μm) were purchased from Specialty Testing and Development Co., York, Pennsylvania. These strips have two legs that are varnished on opposite sides, such that the Cu film grows only on one side of each leg, and film stress will bend the legs in opposite directions. The ABS test strips were cut from 0.5 mm thick ABS sheet

(CS Hyde Company, Lake Villa, Illinois) to the same shape and size as the metal strips. Prior to cutting and desmearing, the sheet was sanded with 600 grit abrasive paper on both sides to achieve a dull and even finish. To grow copper only on one side of each leg, during activation opposite sides were covered with adhesive tape (3 M, type 851). Following a procedure described elsewhere, the spread of the test strips in the images is converted to curvature, allowing for the effect of gravity on the strip shape [11].

To monitor the initial phase of thin film growth, copper was plated on to Pd-activated ABS coupons for times ranging from 1 s to 17 min. Non-specular reflectivity spectra of the plated surface were collected in the range from 400 to 900 nm with a DIVA Series 2 HWL digital spectrometer (Nicholl Education Ltd., Huddersfield, UK). A halogen lamp with a glass filter was used for illumination. Scanning electron micrographs (SEM) were obtained with a JEOL JSM-5600 operated at 10 kV, and an Oxford Inca Energy 200 system was used for elemental analysis of the deposits. Prior to imaging an approximately 10 nm thick gold coating was applied to the surface by plasma sputtering. XPS spectra were obtained, after Ar ion sputtering, with a VG Microtech MultiLab ESCA 2000 System. Film adhesion was evaluated for seven films on ABS substrates with a LumiFrac adhesion analyzer (LUM GmbH, Berlin).

### 3. Results

#### 3.1. Microstructure evolution and composition

Fig. 1 shows selected areas of SEM micrographs (full size images are provided as Supplementary material 1) and optical images of ABS surfaces before and after plating. The desmearing process removes the butadiene component of the ABS copolymer at the surface, creating the pores seen in the micrograph of the desmeared ABS. A palladium seed layer is deposited on the desmeared ABS to initiate the autocatalytic copper plating. Randomly distributed Pd particles with a typical separation of 100 nm are just resolved in the micrograph. After 1 s of electroless Cu plating many more particles are visible on the surface, which shows that only the largest Pd nuclei were visible before plating. Images of samples plated for 1, 5 and 10 s exhibit isolated particles whose number and size dispersion increases with time, confirming that initially many of the active Pd nuclei were unresolved in the micrograph. The image after 30 s shows that the particles have merged. The nascent Cu film also leads to a reduced image contrast relative to the isolated particles. The image after 1 min of plating already shows new Cu particles growing at the surface of the continuous film. The pores created by the desmearing process are partially covered after 2 min of plating, with coverage being complete after 17 min of plating. These last two images also show a cauliflower morphology, with the growth of new copper particles being initiated continuously at the surface of large particles. Imaged cross sections (not shown) demonstrate a dense film that is almost void-free. Film resistivity was measured with the four-probe technique for nine samples with  $0.1 \mu\text{m} \leq h_f \leq 5.65.6 \mu\text{m}$ . The average value,  $1.7 \pm 0.5 \mu\Omega \cdot \text{cm}$ , is consistent with the bulk resistivity of copper ( $1.72 \mu\Omega \cdot \text{cm}$ ).

The optical images (Fig. 1, bottom) can be characterized by three overlapping stages. The color of the ABS substrate is visible until 5 s of plating. Areas with a dark color in the images from 1 to 60 s correspond to the copper nanoparticles. The red hue of copper, seen from 30 s onwards, corresponds to the merged copper particles that evolve towards the continuous film. This is confirmed by reflectivity measurements of the same samples as a function of wavelength (Fig. 2). As the ABS is covered initially by Cu nanoparticles, the reflectivity is reduced until a minimum is reached after about 10 s of plating. Absorbance of nanocrystalline copper particles by Hussain and Pal [15] agrees qualitatively with the present results. In a quantitative analysis, they attribute the reduced reflectivity at 700 nm (peak range from about 600 to 800 nm) to Mie scattering. A narrow dip in the reflectivity curves at about 480 nm after one second of deposition, red-shifted to 500 nm

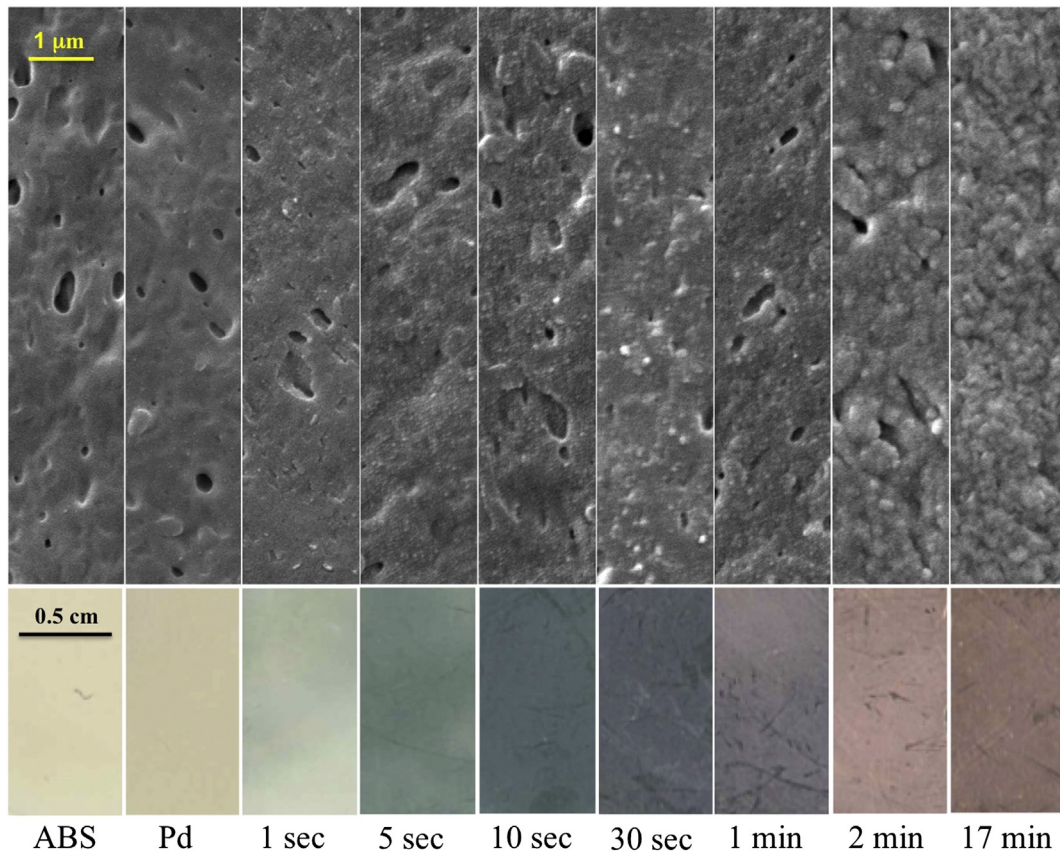


**Fig. 1.** SEM micrographs (top) and optical images (bottom) of desmeared ABS, ABS with Pd nuclei and ABS plated with Cu for the indicated times. (For interpretation of the references to color in this figure, the reader is referred to the web version of this article.)

for the spectra at 5 and 10 s, may be due to the excitation of surface plasmon modes [16]. After 17 min the Cu film shows the typical high reflectivity in the long wavelength range, with high absorption below about 2.0 eV due to excitation of electrons to the 3d electronic bands [17]. Enhanced reflectivity in the red is seen first after plating for 30 s,

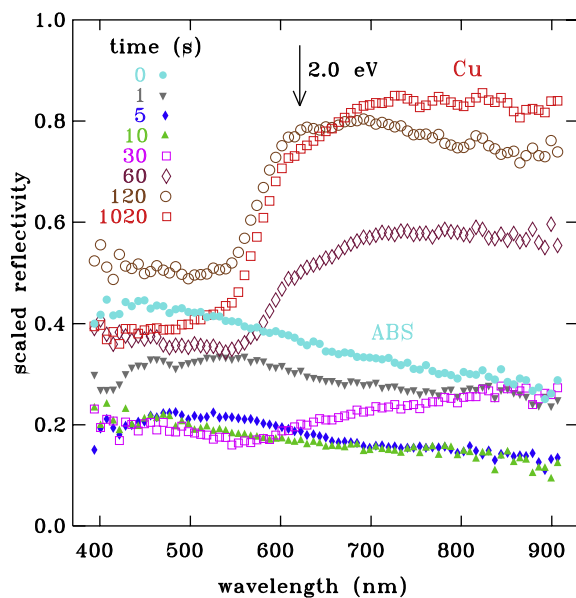


**Fig. 2.** Diffuse reflectivity of copper films plated for the indicated times as a function of wavelength. Zero and one correspond to the signals from black and white paper, respectively. (For interpretation of the references to color in this figure, the reader is referred to the web version of this article.)

matching the merging of the particles in the SEM micrograph. The non-spectral purple color perceived for the film at this stage can be attributed to the combination of the Mie scattering by Cu nanoparticles, the dominant effect after 1 and 5 s of plating, and the metallic reflectivity of the emerging Cu film from 30 s onwards.

Fig. 3 shows the composition  $x$  of  $\text{Cu}_{100-x}\text{Ni}_x$  films deposited on ABS at 32 °C for times ranging from 15 s to 120 min, plotted as a function of film thickness. At the start of the plating process the nickel

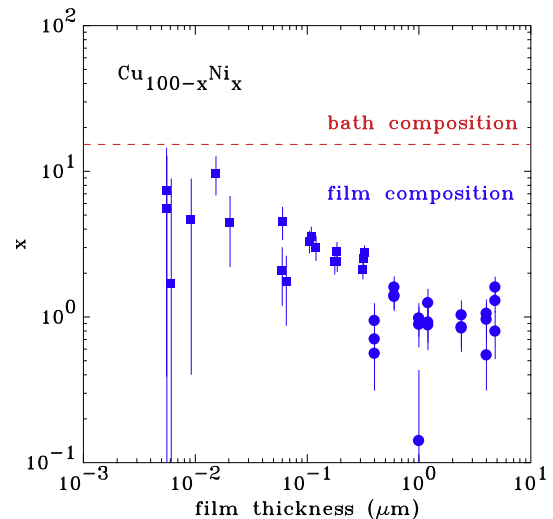


**Fig. 3.** Nickel content of  $\text{Cu}(\text{Ni})$  films on ABS as a function of film thickness, sampled in three spots for each film. The measurement samples approximately a 0.3 μm thick top layer of the film. For thin films, the thickness is based on the strength of the Cu EDS signal (squares), and for thick films the thickness is calculated from the plating time (circles).

concentration in the film ( $x \approx 6$ ) is about half of the concentration ratio in the bath,  $x = 13.0$ . The metal transfer from the bath to the film becomes increasingly non-stoichiometric with increasing plating time/film thickness, and films thicker than  $1.0 \mu\text{m}$  have the approximate composition  $\text{Cu}_{99}\text{Ni}_1$ .

Three-dimensional spatial maps of the nickel distribution in electroless Cu films, for a bath formulation that is similar to the one considered here have been obtained with time-of-flight secondary ion mass spectrometry. These unpublished data confirm the assumption in Ref. [8] that the Ni atoms segregate at GBs. More specifically, these maps show that nickel precipitates are located along the lines and points where several GBs meet. XPS measurements were carried out on a sample deposited for 1 min after Ar ion sputtering. We observe a  $\text{Ni}2p_{3/2}$  peak at a binding energy of 856 eV (Supplementary material 2). Position and shape of this peak matches reference spectra for  $\text{Ni}(\text{OH})_2$  [18,19]. XPS peaks of metallic Ni are not present in the spectrum, but additional broader peaks at high binding energies (864, 876 and 884 eV) could not be assigned. We conclude that the co-deposited nickel is present as a hydroxide in the GBs [20]. Since  $\text{Ni}(\text{OH})_2$  is, unlike metallic Ni, not soluble in the surrounding fcc-Cu crystals, the Ni co-deposits remain in the GBs, where they reduce the mobility of the Cu atoms as discussed below.

### 3.2. Time evolution of average film stress

Fig. 4 shows the average stress of Cu films plated on (a) ABS and (b) metal substrates at  $32^\circ\text{C}$ . For all films, the stress is tensile (positive) during and after plating. The stress of films plated on ABS substrates decreases monotonically during plating. Sample-to-sample variations are high during the first 6 min of plating. After deposition, three processes take place: upon draining the bath, stress decreases immediately towards compressive (1). This prompt change is followed by a further, more gradual relaxation towards compressive (2). Then a slower process raises the stress again (3). Due to the counteracting trends (2) and (3), the stress assumes a minimum during relaxation.

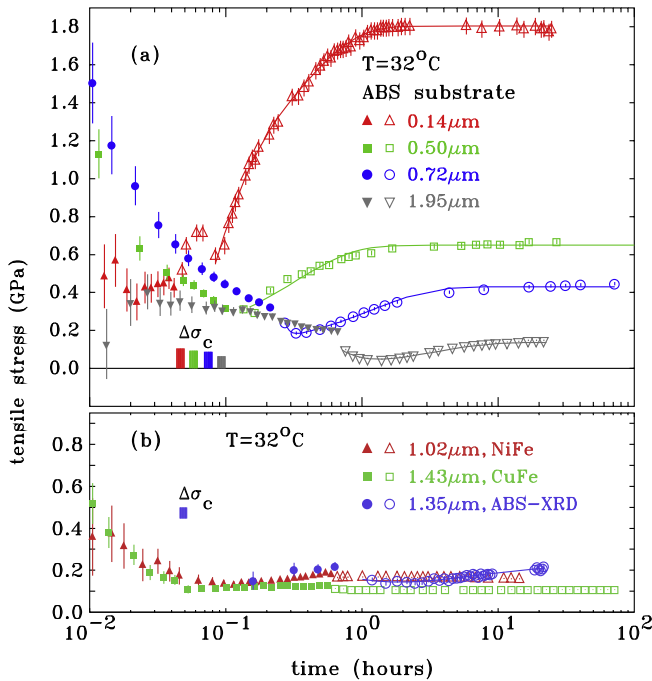


**Fig. 4.** (a) Stress as a function of time for the copper films plated onto ABS substrates. Closed and open symbols show data during and after plating, respectively. Solid lines are numeric fits to the data.  $\Delta\sigma_c$ , shown by bars, is the calculated decrease in stress change upon termination of film growth due to differential thermal contraction of ABS and Cu. (b) Same for plating onto metal substrates, and stress calculated from XRD based strain.

Equilibrium is reached after about 10 h. Comparing films of different thickness [Fig. 4(a)] shows that this relaxation is faster and more pronounced for the thinner films.

The stress calculated from the XRD based crystallite strain in Fig. 4(b) shows the same relaxation pattern with a smaller amplitude (for details refer to Section 3.4). Films plated on metal substrates [Fig. 4(b)] attain a nearly constant stress after about  $\sim 6$  min of plating. Stress remains nearly unchanged during the rest of the plating interval, as well as after plating. The data for two types of metal substrates agree. Final stress on metal and ABS substrates is tensile and of similar magnitude. Since the stress behavior for films on metal and ABS differs qualitatively, any judgment of stress based on metal substrates is inapplicable for deposition on ABS.

For ABS substrates, the prompt change of the stress towards compressive upon draining the bath is caused by the thermal contraction of the substrate relative to the copper as the temperature changes from bath temperature to room temperature. The magnitude of this jump,  $\Delta\sigma_c$ , depends on the temperature change  $\Delta T$ , the thermal expansion coefficients, the elastic constants and the thicknesses of film and substrate. Temperature-induced stress changes of the substrate/film composites, calculated according to the expression given by references [21,11], are shown by vertical bars in Fig. 4(a) and (b). The calculated and the observed stress changes agree within the experimental uncertainties. For films thinner than  $0.72 \mu\text{m}$ , the effect of the substrate contraction on film stress is not well resolved. In the case of metal substrates, the coefficients of thermal expansion of films and substrates are small, and accordingly we do not observe a jump in the stress at the end of plating in Fig. 4(b).

Relaxation of the copper film on ABS after the end of deposition, at time  $t_1$ , is characterized by a decrease of the stress towards a minimum, followed by an increase towards an equilibrium value. In Fig. 4 the average stress decreases during deposition. Accordingly, the stress at the start of the relaxation process,  $\sigma_i$ , also decreases with increasing film thickness. The time dependence of the stress after the end of plating (considered here to be  $t = 0$ ) can be parameterized as

$$\sigma(t) = \sigma_\infty - \Delta\sigma_1 e^{-t/\tau_1} + \Delta\sigma_2 e^{-t/\tau_2}, \quad (2)$$

where  $\sigma_\infty$  is the equilibrium stress reached after a sufficiently long relaxation time,  $\Delta\sigma_1$  is the amplitude of the stress decrease,  $\Delta\sigma_2$  is the amplitude of the slower stress increase, and  $\tau_1$  and  $\tau_2$  are the corresponding time constants. Numeric fits of the post-deposition data to Eq. (2), shown as solid lines in Fig. 4, describe the data well. Fig. 4 shows that the thinner films have larger relaxation amplitudes. For this reason, Fig. 5 shows the adjustable parameters of Eq. (2) as a function of film thickness. Since the figure combines data from films deposited at different temperatures, we see that in the present case temperature and film deposition rate have no noticeable effect on strain. Therefore, atomic mobility is sufficient for the deposition process to take place in a steady state regime [7]. The final film stress,  $\sigma_\infty$ , decreases monotonically with film thickness (Fig. 5). The stress at  $t = 0$ ,  $\sigma_i = \sigma_\infty - \Delta\sigma_1 + \Delta\sigma_2$ , also decreases with film thickness, in agreement with the stress decrease during plating in Fig. 4. This suggests the presence of a layer of high tensile stress at the film-substrate interface, with lower stress in the remainder of the deposit. This is discussed in Section 3.3, where we consider the stress profile within the films.

The final stress is on average about twice the initial stress, and the increase is mostly due to the larger change  $\Delta\sigma_2$ . The time constant  $\tau_2$  of this slow relaxation towards tensile is typically 1 h, but it increases with film thickness [Fig. 5(b)]. The dependence of the relaxation rate on film thickness indicates that adatom diffusion to the film surface contributes to the post-deposition relaxation process, as the chemical potential at the film surface is first higher than in the GB during deposition and then lower after the adatom flow to the surface has stopped [7]. This relaxation is typical for metal films with high atomic mobility, where the diffusion of Cu atoms to favorable positions in the

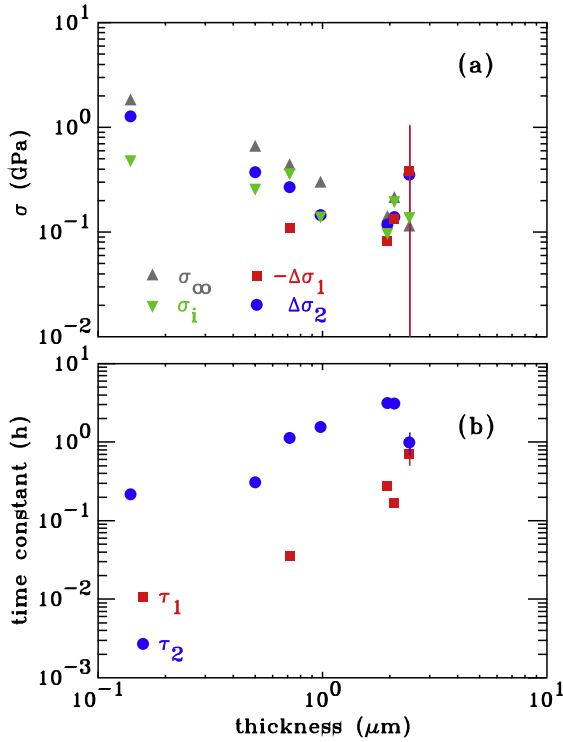


Fig. 5. (a) Initial deposit stress,  $\sigma_i$ , equilibrium stress  $\sigma_\infty$ , and the amplitudes  $\Delta\sigma_1$  and  $\Delta\sigma_2$  of the fast and slow relaxation processes as a function of film thickness. (b) Time constants  $\tau_1$  and  $\tau_2$  of the fast and slow relaxation processes.

GBs or to the film surface creates free volume [6], generating tensile strain. We have observed this relaxation previously in nickel-free electroless Cu films, whereas in films with small amounts of co-plated nickel this relaxation process is partially or fully suppressed [5,8]. Clearly, although Ni has been co-deposited, in the present films the Cu atoms in the GBs have retained some of their mobility.

Next we consider the relaxation process that takes place right after the thermally induced stress change. It is towards compressive and relatively fast, with  $\tau_1$  varying from less than 1 min for films thinner than  $1 \mu\text{m}$  to less than 1 h for the thickest films considered here [Fig. 5(b)]. Accordingly, this process is not sufficiently resolved for numeric analysis in the stress data of most of the thinner films. When plating from a bath with constant post-plating stress onto ABS, we were able to observe this fast relaxation by itself [11]. We attribute this relaxation to the mechanical yielding of ABS near the ABS-Cu interface, releasing the strain energy build up by the tensile copper film. Mechanical relaxation of ABS at ambient temperature takes place on a time scale of about 20 min [22].

In Fig. 5(a), the initial stress  $\sigma_i$  and the final stress  $\sigma_\infty$  decrease, to a good approximation, linearly with film thickness. Therefore the stress-thickness product,  $h_f\sigma$ , is approximately constant for samples of different thickness. At the end of relaxation the values are quite tightly distributed with  $h_f\sigma_\infty = 3.1 \pm 0.6 \text{ N/cm}$ , whereas at the end of deposition the product for the different samples still varies, with  $h_f\sigma_i = 2.3 \pm 1.3 \text{ N/cm}$ . This suggests that the stress is limited by the maximum force/length that the ABS substrates can sustain without further mechanical yielding at the ABS-Cu interface. We attribute the increase of the stress-thickness product with time to work hardening of the substrate and a correspondingly modified stress gradient in the ABS.

The Ni concentration in Fig. 3 is correlated with the stress values and stress relaxation amplitudes in Fig. 5(a). We attribute this correlation to the varying volume fraction of grain boundaries. The lower Ni content of the thicker films reflects the lower volume fraction of GBs. GBs are both

the origin of film stress and the locus of stress relaxation, so that the larger volume fraction of GBs in thinner films give rise to more and faster relaxation processes [23].

### 3.3. Local stress

If the relaxation of the films during plating is sufficiently small, then the spatial distribution of stress can be determined based on the substrate curvature changes. The stress thickness product is  $\sigma(h)h(t) = \int_0^{h(t)} \sigma(x, t) dx$ , where during plating the film thickness  $h(t)$  increases with time  $t$  and  $\sigma(x, t)$  is the in plane stress at the distance  $x$  from the substrate. Differentiating both sides of this equation gives

$$\frac{d}{dh}[\sigma(h)h(t)] = \sigma(h) + \frac{1}{dh/dt} \int_0^{h(t)} \frac{\partial}{\partial t} \sigma(x, t) dt \approx \sigma(h), \quad (3)$$

where the approximation corresponds to disregarding relaxation,  $\frac{\partial}{\partial t} \sigma(x, t) dt = 0$ , of the already deposited copper during plating.

Stress profiles calculated with Eq. (3) are shown in Fig. 6. Films plated on ABS grow with moderate tensile stress, which is highest at the substrate-film interface. Beyond  $\approx 0.7 \mu\text{m}$ , further layers grow with a constant stress of about 0.15 GPa. The bath temperature and hence the plating rate do have no discernible effect on the stress profile.

Local stress of films on metal substrates, shown in Fig. 6(b), is significantly different near the film-substrate interface. The region of initial high tensile stress is narrower than in the case of ABS, and it is followed by a region of compressive stress around  $0.05 \mu\text{m}$ . The stress of subsequent layers approaches the value seen on ABS, 0.15 GPa, from below until a constant stress regime is reached at a thickness of  $0.2 \mu\text{m}$ . The data obtained on two different types of metal substrates agree. Local stress data for each combination of plating bath and substrate are reproducible, but comparison with previous work shows that different stress distribution patterns emerge for each combination [10,11]. A common feature of Ni-free films on metal substrates is a small region of compressive stress at the interface, followed by a region of tensile stress. Stress on ABS substrates is generally tensile, and either constant or decreasing with distance from the interface.

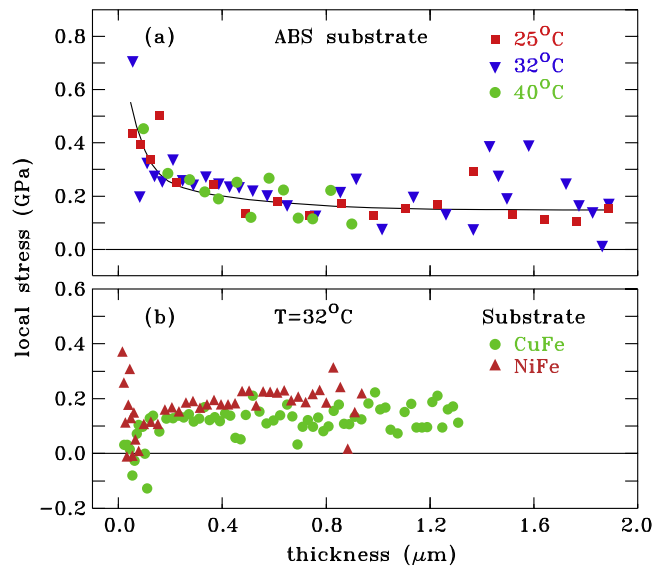


Fig. 6. Variation of local stress with distance from the ABS-Cu interface for films plated on (a) ABS (b) metal substrates at the indicated bath temperatures. The solid line is a guide to the eye.

3.4. Strain analysis with XRD

For a polycrystalline film, strained biaxially within its plane, the observed lattice constant depends on the angle  $\psi$  from the plane normal according to

$$a(\psi) = a_{\perp} + (a_{\parallel} - a_{\perp})\sin^2\psi. \tag{4}$$

Here  $a_{\perp} = a(\psi = 0^\circ)$  is the lattice constant observed in the direction perpendicular to the plane of the film and  $a_{\parallel} = a(\psi = 90^\circ)$  is the lattice constant within the film plane. The dependence of the observed lattice constant on  $\sin^2\psi$  corresponds to the fact that upon flipping the film by  $180^\circ$  one expects the same result. Lattice constants, obtained by least-square fitting of the diffraction peaks of films prepared at  $32^\circ\text{C}$  with different thickness, are shown in Fig. 7. The positive slopes show that the strain of the Cu crystallites is tensile (stretched within the plane of the film). Similar to the stress in Fig. 4, with increasing film thickness, strain decreases. Therefore, the thickness dependence of the XRD-based strain and the substrate curvature based stress agree.

For biaxial stress and elastic behavior, stress and strain (as observed by the lattice constants) are related by

$$\sigma = \frac{E}{1 + \nu} \frac{a_{\parallel} - a_{\perp}}{a}, \tag{5}$$

where  $E$  is Young's modulus,  $\nu$  is Poisson's ratio,  $a$  is the unstrained lattice constant and  $E/(1 + \nu) = 73.8$  GPa for copper [24]. Fig. 8(a) shows the stress calculated from the XRD strain using Eq. (5) and substrate curvature based stress. For films thicker than about  $1\ \mu\text{m}$ , average film stress and crystallite strain are consistent with the elastic behavior of bulk copper. However, for thinner films the stress indicated by the substrate curvature is higher than the stress of the crystallites. This may be due to the additional contributions from the grain boundary regions and the region of high tensile stress at the substrate-film interface (Fig. 6).

For elastic behavior, the angle  $\psi_0$  at which the lattice constant in Eq. (4) equals that of the unstrained film is given by  $\sin^2\psi_0 = 2\nu / (1 + \nu) \approx 0.50$  ( $\nu \approx 0.33$ ) [25]. Since the straight lines in Fig. 7 intersect close to this point, the lattice constants of the (hypothetically) unstrained films remain approximately independent of sample

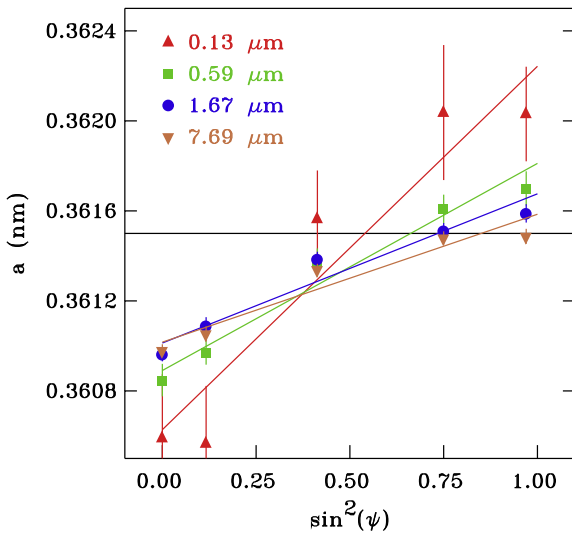


Fig. 7. Lattice constant  $a$  as a function of  $\sin^2\psi$  for copper films with various thicknesses. The horizontal line indicates the bulk lattice constant for copper, and solid lines are the linear fits to the data.

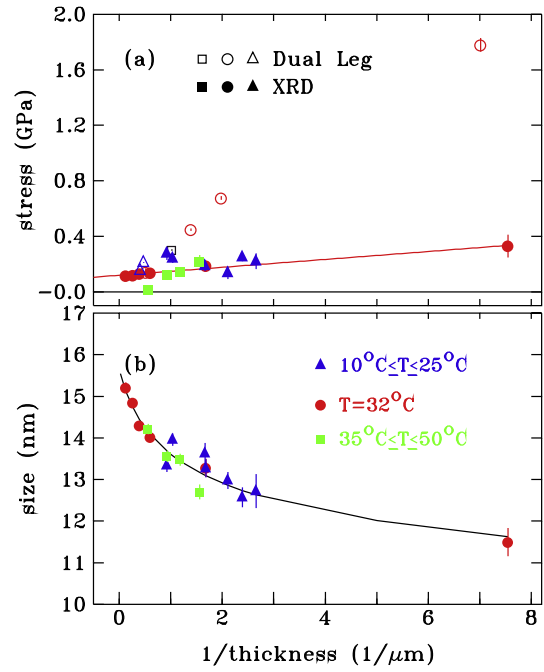


Fig. 8. Variation of (a) stress and (b) crystallite size in copper films with inverse thickness at various bath temperatures. Solid lines are guides to the eye.

thickness. This contrasts with previous work, where upon varying the Ni content in the bath, the lines intersect near  $\sin^2\psi = 2/3$  [8].

The widths of the diffraction peaks, after correction for the diffractometer resolution, correspond to the size of the coherent regions in the Cu crystallites. The crystallite size, determined by Scherrer equation [24], decreases monotonically with inverse thickness [Fig. 8(b)]. Therefore thicker films are, on average, more coarse-grained. Consistent with the desired fine-grained copper microstructure, the XRD-based grain size asymptotically approaches a value below 16 nm in the limit of infinite film thickness.

Fig. 9 shows the time evolution of the lattice constant based on the Cu (311) interplanar spacing observed at the sample orientations  $\psi = 0^\circ$  and  $\psi = 65^\circ$ . Here only the 311 peak was measured in order to maximize the time resolution during the plating interval. A 2θ offset, determined by fitting all peaks after 10 h, was applied to the data. The

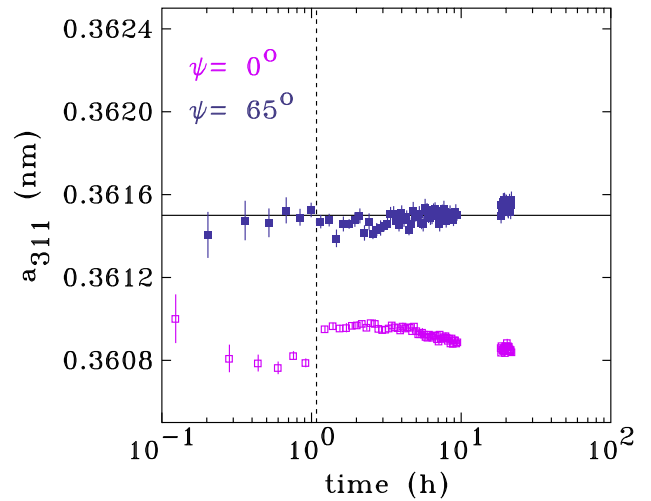


Fig. 9. Time evolution of Cu (311) lattice constant with the sample tilted by  $0$  and  $65^\circ$  (open and closed symbols, respectively) for a film obtained at  $32^\circ\text{C}$ . Time is measured from the filling of the cell. The dotted line indicates the end of plating.

values of  $a_{311}(\psi = 0^\circ)$  and  $a_{311}(\psi = 65^\circ)$  are, respectively, below and approximately equal to the bulk Cu lattice constant of 0.3615 nm. The difference corresponds, by Eq. (4) to tensile strain. As the stress in Fig. 4, strain increases over several hours after plating. During plating the strain remained effectively constant. When plating stopped, the temperature decreases to room temperature, and the substrate contracts more than the film (discussed in Section 3.2). This compressed the film, and we see this in the data at  $\psi = 0^\circ$ .

### 3.5. Texture

Electroless copper films can exhibit a preferred orientation. For a quantitative analysis, we calculate normalized peak intensities

$$NPI(hkl, \psi) = \frac{i(hkl, \psi) / \sum_{h'k'l'} i(h'k'l', \psi)}{I(hkl) / \sum_{h'k'l'} I(h'k'l')}, \quad (6)$$

where  $i(hkl, \psi)$  are the observed peak intensities at sample tilt  $\psi$  and  $I(h'k'l')$  are the expected powder diffraction intensities from ICDD-JCPDS entry #04-0836, with 100, 46, 20, 17 and 5% for  $(hkl) = (111)$ , (200), (220), (311) and (222), respectively. The sums are taken over the first five diffraction peaks [26]. We normalize the data further with respect to  $\psi$  to partially correct the dependence of the diffraction signal on the combination of  $\psi$  and  $2\theta$  according to

$$npi(hkl, \psi) = NPI(hkl, \psi) \frac{\sum_{\psi'} 1}{\sum_{\psi'} NPI(hkl, \psi')}, \quad (7)$$

where the summation is over the five  $\psi$  values at which measurements were made ( $\psi = 0, 20, 40, 60$  and  $80^\circ$ ). Random grain orientation corresponds to  $npi(hkl, \psi) = 1$ . Fig. 10(a) shows  $npi(hkl, \psi)$  for the film exhibiting largest deviation from isotropy, with the (220) intensity enhanced in normal to the film ( $\psi = 0$ ).

Fig. 10(b) shows  $npi(hkl, \psi = 0)$  as a function of film thickness. The normalized (111) and (222) signals would agree if the normalization procedure was correcting all biases of the scattering geometry. In actual fact the (111) signal is larger, but both the (111) and (222) intensities decrease with increasing film thickness. Films less than 0.05  $\mu\text{m}$  thick have close to random crystallite orientation, corresponding to isotropic grain orientation at the beginning of plating. These are also the films with relatively high Ni content. Thicker films exhibit increased (220)

scattering perpendicular to the film surface, corresponding to  $\langle 110 \rangle$  texture, with a maximum near 2  $\mu\text{m}$  film thickness. The preponderance of  $\langle 311 \rangle$  oriented crystals also increases monotonically with film thickness, and it reaches about equal weighting with the  $\langle 110 \rangle$  oriented crystallites for the thickest film considered.  $\langle 110 \rangle$  grain orientation has been referred to as “outward growth”, because the most densely populated rows of atoms in the fcc structure are aligned perpendicular to the surface [27]. A change of preferred orientation from  $\langle 111 \rangle$  to  $\langle 110 \rangle$  with increasing film thickness has been reported for sputtered and electrodeposited Cu films [28,29]. Addition of dipyriddy, the stabilizer in the present bath, has been seen to increase the  $\langle 111 \rangle$  orientation [30].

### 4. Discussion

The bath formulation investigated here was designed for horizontal plating, optimized for superior adhesion on bare resins and good copper surface distribution on IC substrates. Further requirements are blister-free films with low stress and fine-grained structure. The horizontal plating process requires high deposition rates, with a typical plated thickness of 0.8  $\mu\text{m}$ . The experiments described here have probed the Cu film properties inside and outside the specified range of bath operating parameters.

The ionic palladium activation employed with the process studied here enables the plating of thin lines. This performance is consistent with the high spatial density of growing Cu islands in Fig. 1 that are evenly distributed with an observed spacing of about 50 nm, demonstrating a prompt and even plating start. A dark purple hue of the film after 30 s of plating coincides with the appearance of a continuous film in the SEM image. For blanket copper films, good mechanical anchoring to the substrate is achieved by filling of the 200 nm wide pores in the desmeared substrate. Pore filling is nearly complete after 120 s of plating.

Compressive film stress is detrimental because it leads to blistering if the peel strength of the film is insufficient, whereas low to moderate tensile stress is usually unproblematic. Conformal plating of vias requires simultaneous deposition of copper on copper, glass and polymer surfaces. For films with the target thickness of 0.8  $\mu\text{m}$ , the final tensile stress is about 0.3 GPa and 0.15 GPa on ABS and metal surfaces, respectively (Fig. 4), with the difference arising from the stress distribution at the substrate-film interface (Fig. 6). Generally, tensile stress is high at the interface for both substrate types, but in the case of metal substrates this is followed by a narrow zone of compressive stress. Beyond a typical distance of 0.2  $\mu\text{m}$  from the film-substrate interface, stress during growth is about 0.15 GPa for all substrates.

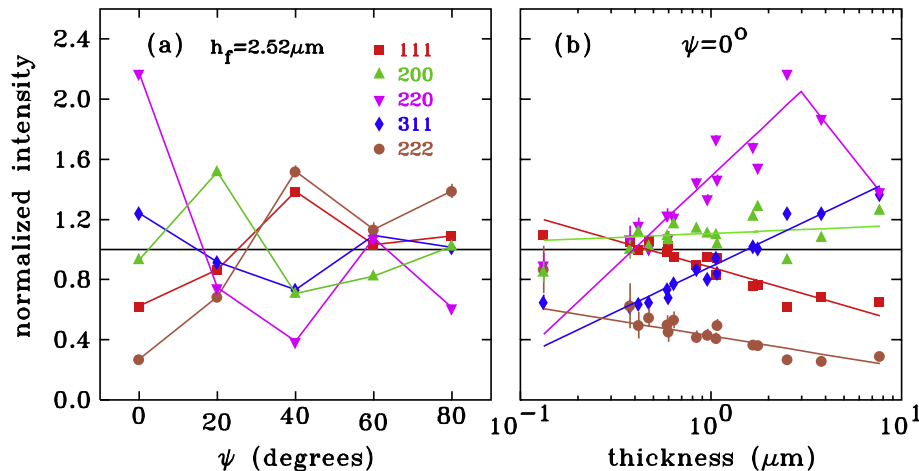


Fig. 10. (a) XRD normalized peak intensities as a function of sample tilt for a 2.52  $\mu\text{m}$  thick film. (b) Normalized peak intensity at  $\psi = 0^\circ$  (preferred orientation) as a function of film thickness. Solid lines are the linear fits to the data.

Independent of substrate type, we see the moderate tensile stress that is a sign of films that adhere well to the substrate.

The stress of films plated on metal is found to be constant after plating is complete (Fig. 4(b)), whereas films on ABS substrates first relax towards compressive and then towards tensile (Fig. 4(a)). This is mirrored, to a lesser extent, in the XRD lattice constants (Fig. 9). Fig. 5 shows that the relaxation amplitudes diminish with plated thickness. As one would expect, the differences seen between metal and ABS substrates vanish as films become thicker.

Stress data on ABS dual leg substrates for two other bath types that we reported previously show considerably less post deposition relaxation than the present case [11]. In Ref. [11], Bath I only relaxed towards compressive with an amplitude of 40 MPa and a time constant of about 15 min, with no relaxation on metal. Bath II on ABS substrates relaxed weakly towards compressive, followed by a slow relaxation towards tensile with an amplitude of 50 MPa or less. Unlike Bath I and the present case, Bath II relaxed noticeably on metal substrates with an amplitude of 125 MPa. To summarize, compared to films on metal substrates, films from the same plating baths on ABS substrates are more prone to successive relaxation processes. However, amplitudes and time constants of these relaxation processes are highly dependent on the bath formulation.

The results in Fig. 8 show that the film properties are independent of plating temperature, implying that in the temperature range employed here the same processes are governing the deposition. By extension, a constant activation energy should describe the deposition rate kinetics. The plating rate as a function of temperature,  $r(T)$ , shown in Fig. 11, follows an Arrhenius law with

$$R(T) = R(T_0) \exp \left[ \frac{E}{k_B} \left( \frac{1}{T_0} - \frac{1}{T} \right) \right], \quad (8)$$

where  $T_0 = 305$  K is the standard bath operating temperature,  $k_B$  is Boltzmann's constant and  $E$  is the activation energy. The data in Fig. 11 show that the bath temperature has a wide process window, although the Arrhenius law overestimates the plating rate at low temperatures. The solid line is a numeric fit to Eq. (8) with  $E = 0.71 \pm 0.03$  eV and  $R(305 \text{ K}) = 0.78 \pm 0.04$  nm/s. Therefore the typical application thickness of  $0.8 \mu\text{m}$  is obtained within 17 min.

A framework for thin film stress proposes that the steady-state stress is controlled by the dimensionless factor  $\frac{\sigma}{R}$ , where  $D$  is the

diffusion rate of the adatoms between the film surface and the GBs, and  $L$  is the grain size [7,31]. In the present case, the temperature (and therefore  $R$ ) does not affect the stress, and the steady-state deposition stress  $\sigma_f$  becomes less tensile with increasing film thickness ( $\sigma_f \propto 1/h_f$ ). This is consistent with a low mobility regime during deposition (due to the  $\text{Ni}(\text{OH})_2$  co-deposits in the GBs) with  $\frac{\sigma}{R} \ll 1$ , for which the framework predicts tensile stress that decreases as a function of  $L^{-1/2}$ . Since  $L$  increases with  $h_f$ , our results are in qualitative agreement with this framework.

## 5. Conclusions

Plating start, plating rates, composition, stress and crystallite strain evolution and film texture were investigated for a production-level electroless plating bath that is optimized for blanket copper plating in horizontal plating applications. Key properties of this bath are listed in Table 1. The plating start is prompt, with continuous coverage of the surface after about 30 s. For the ABS substrates used here, the standard thickness of  $0.8 \mu\text{m}$  was attained after 17 min. Comparison of SEM micrographs with photo-spectroscopic data show that a dark purple color impression corresponds to the continuous copper film. The Ni content of the film at the start of plating is about 6%, and it decreases to about 1% as the film thickness increases to  $1 \mu\text{m}$  and more. Ni atoms are segregated at the grain boundaries in the form of hydroxides, and the decreased Ni content of the thicker films reflects a reduced volume fraction of GBs. The larger crystallites near the film surface have preferred  $\langle 110 \rangle$  orientation.

Crystallite strain, determined by XRD, and film stress based on substrate curvature are tensile during and after plating. Tensile stress is highest at the film-substrate interface. On metal substrates, the region of tensile stress is followed by a narrow region of compressive stress located about 50 nm from the substrate. The substrate curvature indicates a higher stress than the crystallite strain if elastic behavior is assumed. The difference is attributed to elastic/inelastic grain boundary sliding. Stress after plating first relaxes quickly towards compressive due to mechanical yielding of the ABS, and then, in a slower process, back towards tensile due to GB relaxation in the Cu film. Relaxation of overall film stress and XRD based crystallite strain follow the same pattern, but again the amplitude of the strain relaxation is smaller. The final film stress and the stress relaxation amplitude decrease with film thickness in a pattern that matches the Ni content. They are correlated because Ni segregation, stress and stress relaxation are associated with the GBs, whose volume fraction decreases with increasing film thickness.

## Acknowledgments

Mr. James Ehrman (Mount Allison University) carried out the SEM imaging and EDS measurements. We thank Mr. Andrew George and Prof. Theodore Monchesky for the XPS analysis. The XPS facility at the Institute for Research in Materials, Dalhousie University, is supported by the Canada Foundation for Innovation, the Atlantic Innovation Fund and other sources.

## References

- [1] W. Sha, X. Wu, K.G. Keong, *Electroless Copper and Nickel-phosphorus Plating: Processing, Characterisation and Modelling*, Woodhead Publishing, Cambridge UK, 2010.
- [2] M. Paunovic, *Electroless deposition of copper*, in: M. Schlesinger, M. Paunovic (Eds.), *Modern Electroplating*, Wiley & Sons, NY 2000, pp. 645–665 (Ch. 17).
- [3] L. Yu, L. Guo, R. Preisser, R. Alkolkar, *Autocatalysis during electroless copper deposition using glyoxylic acid as reducing agent*, *J. Electrochem. Soc.* 160 (12) (2013) D30046–D33008.
- [4] P. Shi, J. Wu, *High density copper nucleation on ruthenium and its applications to direct plating of advanced interconnects*, *ECS Trans.* 52 (11) (2013) 437–442.
- [5] R. Brüning, B. Muir, E. McCalla, E. Lempereur, F. Brüning, J. Etkorn, *Strain in electroless copper films monitored by x-ray diffraction during and after deposition and its dependence on bath chemistry*, *Thin Solid Films* 519 (2011) 4377–4383.

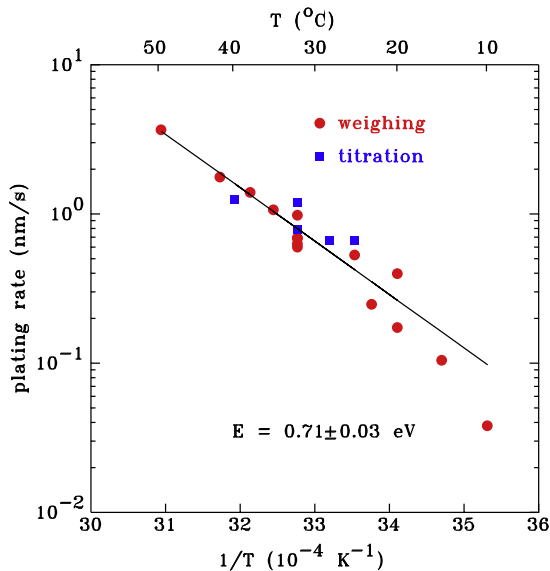


Fig. 11. Plating rate as a function of inverse temperature. Film thickness was evaluated by dissolving and titrating the deposited copper or by weight change. The solid line as a numeric fit to an Arrhenius law.

- [6] E. Chason, B.W. Sheldon, L.B. Freund, J.A. Floro, S.J. Hearne, Origin of compressive residual stress in polycrystalline thin films, *Phys. Rev. Lett.* 88 (2002) 156103.
- [7] E. Chason, A kinetic analysis of residual stress evolution in polycrystalline thin films, *Thin Solid Films* 526 (2012) 1–14.
- [8] S. Bamberg, L.K. Perry, B. Muir, A. Abuzir, F. Brünig, R. Brünig, The effect of nickel on the strain evolution in chemical copper films, *Thin Solid Films* 520 (23) (2012) 6935–6941.
- [9] Y. Yang, H. Huang, S.K. Xiang, E. Chason, Stress control in polycrystalline thin films—reduction in adatoms diffusion into grain boundaries via surfactants, *Appl. Phys. Lett.* 96 (21) (2010) 211903.
- [10] T. Sharma, R. Brünig, C. Brown, A. Sibley, J. Etzkorn, Stress and strain evolution in electroless copper films evaluated with x-ray diffraction and substrate curvature, *J. Electrochem. Soc.* 160 (6) (2013) D226–D232.
- [11] R. Brünig, A. Sibley, T. Sharma, D. Brown, T. Demay, F. Brünig, T. Bernhard, Stress of electroless copper deposits on insulating and metal substrates, *Thin Solid Films* 565 (2014) 136–142.
- [12] M. Cordill, O. Glushko, J. Keith, V. Marx, C. Kirchlechner, Measuring electro-mechanical properties of thin films on polymer substrates, *Microelectron. Eng.* 137 (2015) 96–100.
- [13] J. Weissmüller, J. Markmann, M. Grewer, R. Birringer, Kinematics of polycrystal deformation of grain boundary sliding, *Acta Mater.* 59 (11) (2011) 4366–4377.
- [14] L. Freund, S. Suresh, *Thin Film Materials: Stress, Defect Formation and Surface Evolution*, Cambridge University Press, New York, NY, 2003.
- [15] S. Hussain, A. Pal, Surface plasmon effect in nanocrystalline copper/dlc composite films by electrodeposition technique, *Bull. Mater. Sci.* 29 (6) (2006) 553–557.
- [16] S. Link, M. El-Sayed, Shape and size dependence of radiative, non-radiative and photothermal properties of gold nanocrystals, *Int. Rev. Phys. Chem.* 19 (3) (2000) 409–453.
- [17] R. Courths, S. Hüfner, Photoemission experiments on copper, *Phys. Rep.* 112 (2) (1984) 53–171.
- [18] K. Kishi, T. Fujita, Interaction of Ni/Cu(100) surfaces with O<sub>2</sub> studied by XPS, *Surf. Sci.* 227 (1–2) (1990) 107–113.
- [19] A.P. Grosvenor, M.C. Biesinger, R.St.C. Smart, N. Stewart McIntyre, New interpretations of XPS spectra of nickel metal and oxides, *Surf. Sci.* 600 (2006) 1771–1779.
- [20] A. van der Ven, D. Morgan, Y.S. Meng, G. Ceder, Phase stability of nickel hydroxides and oxyhydroxides, *J. Electrochem. Soc.* 153 (6) (2006) A210–A215.
- [21] A. Evans, J. Hutchinson, The thermomechanical integrity of thin films and multilayers, *Acta Metall. Mater.* 43 (2) (1995) 2507–2530.
- [22] A. Gol'dman, A. Freidin, Effect of hydrostatic pressure on the shear strain of acrylonitrile-butadiene styrene plastic, *Mech. Compos. Mater.* 25 (1) (1989) 19–23.
- [23] R. Daniel, E. Jäger, J. Todt, B. Sartory, C. Mittlerer, J. Keckes, Mono-textured nano crystalline thin films with pronounced stress-gradients: on the role of grain boundaries in the stress evolution, *J. Appl. Phys.* 115 (2014) 203507.
- [24] B.D. Cullity, S.R. Stock, *Elements of X-ray Diffraction*, 3rd edition Prentice Hall, NJ, 2001.
- [25] G.C.A.M. Janssen, Stress and strain in polycrystalline thin films, *Thin Solid Films* 515 (2007) 6654–6664.
- [26] W. Zhang, A. Li, G. Ma, K. Yin, Y. Xia, Z. Liu, C. Chan, K. Cheung, M. Bayes, K. Yee, Interpretation of texture changes during self-annealing of electroplated copper, *Microelectron. Eng.* 87 (2010) 2488–2494.
- [27] N. Pangarov, Preferred orientations in electro-deposited metals, *J. Electroanal. Chem.* 9 (1965) 70.
- [28] H. Wei, H. Huang, C. Woo, R. Zheng, G. Wen, X. Zhang, Development of <110> texture in copper thin films, *Appl. Phys. Lett.* 80 (13) (2002) 2290–2292.
- [29] H. Merchant, J. Wang, L. Glannuzzi, Y. Liu, Metallurgy and performance of electrodeposited copper for flexible circuits, *Circuit World* 26 (4) (2000) 7–14.
- [30] J. Li, H. Hayden, P. Kohl, The influence of 2,2'-dipyridyl on non-formaldehyde electroless copper plating, *Electrochim. Acta* 49 (2004) 1789–1795.
- [31] E. Chason, A. Engwall, F. Pei, M. Lafouresse, U. Bertocci, G. Stafford, J.A. Murphy, C. Lenihan, D.N. Buckley, Understanding residual stress in electrodeposited Cu thin films, *J. Electrochem. Soc.* 160 (12) (2013).